Vibrational Response of Nanorods to Ultrafast Laser Induced Heating: Theoretical and Experimental Analysis

6 AUTHORS, INCLUDING:

Gregory V Hartland
University of Notre Dame
148 PUBLICATIONS **6,244** CITATIONS

Paul Mulvaney
University of Melbourne
311 PUBLICATIONS **24,584** CITATIONS

Jorge Pérez-Juste
University of Vigo
214 PUBLICATIONS **7,717** CITATIONS

Vibrational Response of Nanorods to Ultrafast Laser Induced Heating: Theoretical and Experimental Analysis

Min Hu,[†] Xuan Wang,[†] Gregory V. Hartland,*,[†] Paul Mulvaney,[‡]
Jorge Perez Juste,[‡] and John E. Sader[§]

*Contribution from the Department of Chemistry and Biochemistry, University of Notre Dame,
Notre Dame, Indiana 46556-5670, School of Chemistry, The University of Melbourne,
Victoria 3010, Australia, and Department of Mathematics and Statistics,
The University of Melbourne, Victoria 3010, Australia*

Received July 21, 2003; E-mail: hartland.1@nd.edu

Abstract: In this paper, we elucidate the vibrational response of cylindrical nanorods to ultrafast laser-induced heating. A theoretical analysis of the expected behavior is first presented. This analysis predicts that both extensional and breathing vibrational modes of the rods should be excited by laser-induced heating. Analytical formulas are derived assuming that the heating/expansion process is instantaneous, and that the lengths of the rods are much greater than their radii. These results show that the breathing mode dominates the mechanical deformation of the rod. However, because the frequency of the extensional mode is much lower than that of the breathing mode, the extensional mode will dominate the response for a real experiment (a finite-time heating/expansion process). The results of this model are compared to data from transient absorption experiments performed on gold nanorods with average lengths between 30 and 110 nm. The transient absorption traces show pronounced modulations with periods between 40 and 120 ps, which are only observed when the probe laser is tuned to the longitudinal plasmon band. The measured periods are in good agreement with the expected values for the extensional modes of the rods. For rods wider than 20 nm, the breathing mode can also be observed and, again, the measured periods are in good agreement with the theoretical calculations. The breathing mode is not observed for thinner rods (<20 nm width) because, in this case, the period is comparable to the time scale for lattice heating.

1. Introduction

In the past several years, a number of groups have shown that ultrafast laser excitation of nanoparticles can coherently excite low-frequency vibrational modes.[1–9] These observations have been made for metallic[2,4,5,7,8] and semiconducting particles,[1,3,6] as well as for aggregates of metal particles.[9] The excitation mechanism is slightly different for metallic versus semiconducting materials. For semiconductors, the vibrational modes are excited by a displacive mechanism: band-gap excitation changes the dimensions of the unit cell, which can impulsively excite totally symmetric phonon modes.[10] In contrast, for metal particles excitation occurs via the lattice expansion that follows rapid laser-induced heating.[11,12] In both cases, the phonon modes observed are those that correlate with the expansion coordinate of the particle, which for spherical particles is the symmetric breathing mode.[11,12] The measured vibrational frequencies are in excellent agreement with calculations based on continuum elastic theory, for both homogeneous particles[13,14] and heterogeneous core−shell particles.[15] In terms of practical applications, these measurements provide a way of determining the material properties of nanometer sized objects if the dimensions are accurately known, or the dimensions of the objects if the material properties are known.

There have been very few reports of experimental or theoretical results for nonspherical particles, even though there have been tremendous advances in the past several years in synthetic procedures for making particles with different sizes

† Department of Chemistry and Biochemistry, University of Notre Dame.
‡ School of Chemistry, The University of Melbourne.
§ Department of Mathematics and Statistics, The University of Melbourne.

(1) Krauss, T. D.; Wise, F. W. *Phys, Rev. Lett.* **1997**, *79*, 5102.
(2) Nisoli, M.; De Silvestri, S.; Cavalleri, A.; Malvezzi, A. M.; Stella, A.; Lanzani, G.; Cheyssac, P.; Kofman, R. *Phys. Rev. B* **1997**, *55*, R13 424.
(3) Thoen, E. R.; Steinmeyer, G.; Langlois, P.; Ippen, E. P.; Tudury, G. E.; Cruz, C. H. B.; Barbosa, L. C.; Cesar, C. L. *Appl. Phys. Lett.* **1998**, *73*, 2149.
(4) Hodak, J. H.; Martini, I.; Hartland, G. V. *J. Chem. Phys.* **1998**, *108*, 9210.
(5) Del Fatti, N.; Voisin, C.; Chevy, F.; Vallée, F.; Flytzanis, C. *J. Chem. Phys.* **1999**, *110*, 11 484.
(6) Cerullo, G.; De Silvestri, S.; Banin, U. *Phys. Rev. B* **1999**, *60*, 1928.
(7) Perner, M.; Gresillon, S.; Marz, J.; von Plessen, G.; Feldmann, J.; Porstendorfer, J.; Berg, K. J.; Berg, G. *Phys. Rev. Lett.* **2000**, *85*, 792.
(8) Qian, W.; Lin, L.; Deng, Y. L.; Xia, Z. J.; Zou, Y. H.; Wong, G. K. L. *J. Appl. Phys.* **2000**, *87*, 612.
(9) Grant, C. D.; Schwartzberg, A. M.; Norman, T. J.; Zhang, J. Z. *J. Am. Chem. Soc.* **2003**, *125*, 549.

(10) Zieger, H. J.; Vidal, J.; Cheng, T. K.; Ippen, E. P.; Dresselhaus, G.; Dresselhaus, M. S. *Phys. Rev. B* **1992**, *45*, 768.
(11) Del Fatti, N.; Voisin, C.; Christofilos, C.; Vallée, F.; Flytzanis, C. *J. Phys. Chem. A* **2000**, *104*, 4321.
(12) Hodak, J. H.; Henglein, A.; Hartland, G. V. *J. Chem. Phys.* **1999**, *111*, 8613.
(13) Lamb, H. *Proc. London Math. Soc.* **1882**, *13*, 189.
(14) Bullen, K. E.; Bolt, B. A. *An Introduction to Seismology*, 4th ed.; Cambridge University Press: Cambridge, 1985.
(15) Sader, J. E.; Hartland, G. V.; Mulvaney, P. *J. Phys. Chem. B* **2002**, *106*, 1399.

and shapes.[16-26] Perner et al. observed modulations due to coherently excited vibrational modes in silver ellipses,[7] which were produced by deforming spherical particles embedded in a glass.[27] Experiments were performed with the probe laser resonant to either the longitudinal or the transverse plasmon bands, which correspond to electron oscillation along the major or minor axes of the ellipse, respectively.[28,29] Experiments that probed the longitudinal plasmon band showed a modulation with a period that matches $2L/c_l$, where c_l is the longitudinal speed of sound and L is the length. On the other hand, experiments that probed the transverse plasmon band gave $2w/c_l$, where w is the width of the particle.[7] These are the results expected for an expansion/compression wave generated by ultrafast heating.

In a recent communication, we presented initial results for gold nanorods where modulations due to coherently excited vibrational modes were observed.[30] These particles are formed as capped sphero-cylinders with a surfactant coating. Modulations were only observed for experiments that probed the longitudinal plasmon band. The measured period was also found to depend on the probe laser wavelength. This was attributed to polydispersity in the sample. The longitudinal plasmon band shifts to lower frequency (longer wavelength) with increasing rod length, thus, longer probe wavelengths interrogate longer rods. Furthermore, the periods were not consistent with the results of Perner et al., that is, they did not match the values predicted by $2L/c_l$. In this paper, we present a full description of these experiments, and a theoretical treatment of the response of a cylindrical rod to ultrafast heating. The major aim is to provide an assignment for the coherently excited vibrational motion, since this remains an outstanding problem. Issues that pertain to the phase of the modulations, and the contributions from homogeneous and inhomogeneous spectral broadening in these experiments will be dealt with elsewhere.

2. Theory

In this section, we calculate the temporal response of a cylindrical rod following excitation by a thermal pulse. Because in practice the length L of the rod greatly exceeds it radius a, we focus on the limiting case of $L/a \gg 1$. In so doing, we derive explicit analytical formulas for both the deformation and change in volume. We also compare the results of this analytical analysis to rigorous finite element calculations to establish its validity.

(16) Ahmadi, T. S.; Wang, Z. L.; Green, T. C.; Henglein, A.; El-Sayed, M. A. *Science* **1996**, *272*, 1924.
(17) Chang, S. S.; Shih, C. W.; Chen, C. D.; Lai, W. C.; Wang, C. R. C. *Langmuir* **1999**, *15*, 701.
(18) Martin, B. R.; Dermody, D. J.; Reiss, B. D.; Fang, M. M.; Lyon, L. A.; Natan, M. J.; Mallouk, T. E. *Adv. Mater.* **1999**, *11*, 1021.
(19) Peng, X. G.; Manna, L.; Yang, W. D.; Wickham, J.; Scher, E.; Kadavanich, A.; Alivisatos, A. P. *Nature* **2000**, *404*, 59.
(20) Yu, J. S.; Kim, J. Y.; Lee, S.; Mbindyo, J. K. N.; Martin, B. R.; Mallouk, T. E. *Chem. Commun.* **2000**, 2445.
(21) Nicewarner-Pena, S. R.; Freeman, R. G.; Reiss, B. D.; He, L.; Pena, D. J.; Walton, I. D.; Cromer, R.; Keating, C. D.; Natan, M. J. *Science* **2001**, *294*, 137.
(22) Jin, R. C.; Cao, Y. W.; Mirkin, C. A.; Kelly, K. L.; Schatz, G. C.; Zheng, J. G. *Science* **2001**, *294*, 1901.
(23) Jana, N. R.; Gearheart, L.; Murphy, C. J. *J. Phys. Chem. B* **2001**, *105*, 4065.
(24) Peng, Z. A.; Peng, X. G.; *J. Am. Chem. Soc.* **2001**, *123*, 1389.
(25) Sun, Y. G.; Xia, Y. N. *Adv. Mater.* **2002**, *14*, 833.
(26) Maillard, M.; Giorgio, S.; Pileni, M. P. *J. Phys. Chem. B* **2003**, *107*, 2466.
(27) Borek, R.; Berg, K. J.; Berg, G.; *Glastech. Berichte-Glass Sci. Tech.* **1998**, *71*, 352.
(28) Gans, R *Ann. Phys.* **1915**, *47*, 270.
(29) Link, S.; Mohamed, M. B.; El-Sayed, M. A. *J. Phys. Chem. B* **1999**, *103*, 3073.
(30) Hartland, G. V.; Hu, M.; Wilson, O.; Mulvaney, P.; Sader, J. E. *J. Phys. Chem. B* **2002**, *106*, 743.

Scheme 1: Diagram Showing the Fundamental Extensional and Breathing Modes of a Cylindrical Rod[a]

Extensional Mode (Fundamental)

Breathing Mode (Fundamental)
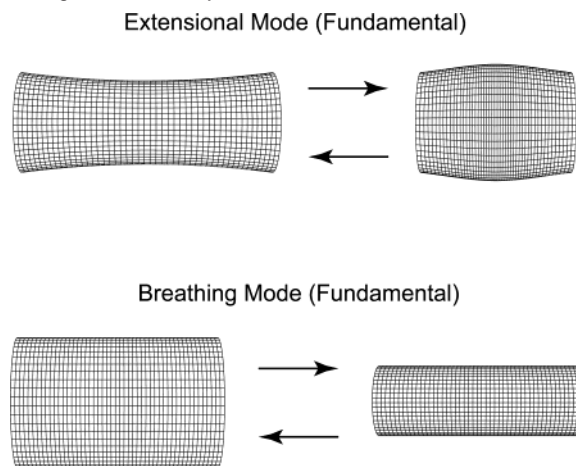
[a] Calculations performed under the assumption that the length greatly exceeds the width. In the breathing mode, a pure radial expansion and contraction is observed; there is no change in length. In the extensional mode, an increase in length is accompanied by a contraction in radius.

Throughout, we assume the rod is composed of a linearly elastic isotropic material.

In practice, the rod is excited by a thermal pulse whose duration is much smaller than the characteristic time scale of rod vibration,[11,12] i.e., the inverse of its fundamental resonance frequency. As such, this thermal pulse can be considered to be of infinitesimal duration. In addition, we assume the rod remains at constant temperature following excitation, because the time scale for heat diffusion from the rod to its surroundings is also typically much longer than the vibrational period.[31,32,33] Consequently, the action of the thermal pulse can be rigorously modeled by the application of an initial uniform strain

$$\mathbf{U}_{t=0} = \epsilon(r\hat{\mathbf{r}} + z\hat{\mathbf{z}}) \tag{1}$$

where $\mathbf{U}$ is the displacement vector, r and z are the radial and longitudinal components of the cylindrical coordinate system, $\hat{\mathbf{r}}$ and $\hat{\mathbf{z}}$ are the unit vectors in the radial and longitudinal directions, ϵ is the magnitude of the initial strain, and t is time. Note that the displacement vector is taken with respect to the final equilibrium state, that is, the average shape of the rod following thermal excitation.

From symmetry, it then follows that in the limiting case of $L/a \gg 1$, only two classes of modes are excited: the extensional and breathing modes of the rod, see Scheme 1. The extensional modes are well studied,[34] and exhibit an axial expansion combined with a radial contraction. As such, these modes probe the Young's modulus of the material. In contrast, the breathing modes exhibit a pure radial expansion and, consequently, probe the bulk modulus of the material. These latter modes are derived in the Supporting Information for this paper.

Decomposing these modes into their spatial and temporal contributions, namely

(31) Mohamed, M. B.; Ahmadi, T. S.; Link, S.; Braun, M.; El-Sayed, M. A. *Chem. Phys. Lett.* **2001**, *343,* 55.
(32) Link, S.; Furube, A.; Mohamed, M. B.; Asahi, A.; Masuhara, H.; El-Sayed, M. A. *J. Phys. Chem. B* **2002**, *106*, 945.
(33) Hu, M.; Hartland, G. V. *J. Phys. Chem. B* **2002**, *106*, 7029; Correction, *J. Phys. Chem. B* **2003**, *107*, 1284.
(34) Love, A. E. H. *A Treatise on the Mathematical Theory of Elasticity*; Dover Publications: New York, 1944.

$$\mathbf{U}_{ext} = \epsilon\mathbf{u}_{ext}(r,z)\exp(-i\omega_{ext}t),$$

$$\mathbf{U}_{br} = \epsilon\mathbf{u}_{br}(r)\exp(-i\omega_{br}t) \quad (2)$$

where the subscripts ext and br shall henceforth refer to the extensional and breathing modes, respectively, it then follows that the spatial dependence of the extensional modes is[34]

$$\mathbf{u}_{ext}(r,z) = \left[-(2n+1)\pi\nu\left(\frac{r}{L}\right)\cos\left((2n+1)\pi\frac{z}{L}\right)\right]\hat{\mathbf{r}} +$$

$$\sin\left((2n+1)\pi\frac{z}{L}\right)\hat{\mathbf{z}} \quad (3)$$

where $n = 0, 1, 2,...$ corresponds to the mode number, and the spatial dependence of the breathing modes is given by (see the Supporting Information)

$$\mathbf{u}_{br}(r,z) = \frac{J_1\left(\frac{\tau r}{a}\right)}{J_1(\tau)}\hat{\mathbf{r}} \quad (4a)$$

where τ satisfies the eigenvalue equation

$$\tau J_0(\tau) = \frac{1-2\nu}{1-\nu}J_1(\tau) \quad (4b)$$

and ν is Poisson's ratio of the rod.

The natural resonant frequencies of the extensional and breathing modes are given by the following respective formulas

$$\omega_{ext}^{(n)} = \frac{2n+1}{L}\pi\sqrt{\frac{E}{\rho}}, \quad (5a)$$

$$\omega_{br}^{(n)} = \frac{\tau_n}{a}\sqrt{\frac{E(1-\nu)}{\rho(1+\nu)(1-2\nu)}} \quad (5b)$$

where τ_n is the n-th root of eq 4b, E is Young's modulus, and ρ is the density of the rod.

Importantly, these modes form a complete orthogonal set correct to $O(a/L)$. This enables the initial uniform strain, eq 1, to be decomposed into these modes, for $L/a \gg 1$. It then follows that the complete temporal response of the rod is given by

$$\mathbf{U}(r,z,t) = \epsilon\sum_n\left[\frac{4(-1)^nL}{\pi^2(2n+1)^2}\mathbf{u}_{ext}(r,z)\cos(\omega_{ext}^{(n)}t) +\right.$$

$$\left.\frac{2(1-\nu^2)a}{(1-\nu)^2\tau_n^2-(1-2\nu)}\mathbf{u}_{br}(r,z)\cos(\omega_{br}^{(n)}t)\right] \quad (6)$$

From eq 6, the temporal response of the change in volume immediately follows

$$\frac{\Delta V}{V} = \epsilon\sum_n\left[\frac{8(1-2\nu)}{\pi^2(2n+1)^2}\cos(\omega_{ext}^{(n)}t) +\right.$$

$$\left.\frac{4(1-\nu^2)}{(1-\nu)^2\tau_n^2-(1-2\nu)}\cos(\omega_{br}^{(n)}t)\right] \quad (7)$$

where ΔV is the change in volume and V is the initial volume of the rod. Equations 6 and 7 are the required results.

In Figure 1, we compare the results of this analytical analysis, which is valid formally for $L/a \gg 1$, to an exact analysis
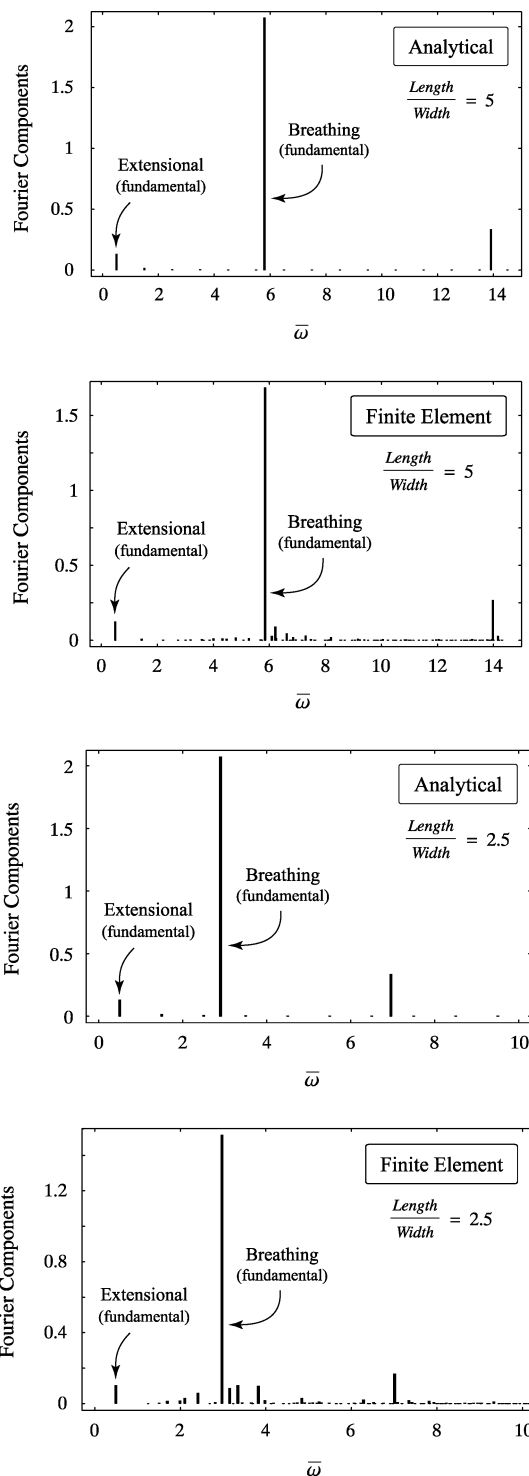

Figure 1. Fourier components for temporal response of change in volume normalized by initial strain ϵ, versus normalized frequency $\bar{\omega} = \omega[L/(2\pi)]\sqrt{\rho/E}$, for a sample with (a) aspect ratio (length/width) = 5 (top two panels) and (b) aspect ratio (length/width) = 2.5 (lower two panels). Bulk material properties for gold are used (Poisson's ratio $\nu = 0.42$). Sum of all normalized Fourier components is 3. The different panels in (a) and (b) show a comparison of the Finite Element and Analytical results. Note that the fundamental extensional mode (first peak) has a very low amplitude in comparison to the fundamental breathing mode (second peak).

obtained using finite element (FE) analysis[35] for gold rods (Poisson's ratio $\nu = 0.42$). FE analysis makes no assumptions

---

(35) LUSAS is a trademark of, and is available from, FEA Ltd., Forge House, 66 High Street, Kingston Upon Thames, Surrey, KT1 1HN, U.K.

about the modes of excitation and picks up all modes. Specifically, we present Fourier components of the change in volume. There are three main peaks in Figure 1 which correspond, in order of increasing frequency, to the fundamental extensional mode, the fundamental breathing mode, and the first overtone of the breathing mode. In terms of the scaled frequency units of Figure 1, the fundamental extensional mode occurs at $\bar{\omega} = 0.5$, the fundamental breathing mode occurs at $\bar{\omega} = 1.160 \times (L/2a)$, and the first overtone of the breathing mode occurs at $\bar{\omega} = 2.782 \times (L/2a)$.

From Figure 1, it is clear that eq 7 gives an accurate representation of the true dynamics of the rod, as calculated by finite element analysis, especially for cases where $L/a \gg 1$ (this is the regime where the above analytical formulas are derived and corresponds to the case encountered in practice). The comparison clearly establishes that the dominant modes excited are the extensional and breathing modes of the rod. The finite element calculations show that other modes are also excited, but their contributions are insignificant in comparison to these dominant modes. Note that the sum of all Fourier components must equal 3ϵ. This explains why the magnitudes of the Fourier components given by eq 7 overestimate the (exact) FE results, because more modes are excited in the exact deformation. Nonetheless, it is clear that the resonant frequencies and amplitudes of the dominant modes are well predicted by the above analytical formulas.

Experimentally, the change in absorption spectrum of the rods is monitored. Rigorous calculations of transient absorption spectra pose a formidable challenge, since solutions of the corresponding electromagnetic problem and knowledge of the dielectric properties of the rod are required. Consequently, such a calculation is not pursued here. However, the transient absorption spectrum is expected to have contributions from both the rod deformation (change in aspect ratio) and its change in volume.[12,30] Thus, as shown by eqs 6 and 7, both the breathing and extensional modes should contribute to the signal. In what follows, the periods extracted from the time-resolved measurements will be directly compared to the resonant frequencies predicted by eq 5, to establish which modes are observed in the experiments.

Interestingly, the above calculations show that the ratio of the resonant frequencies for the fundamental breathing and extensional modes is directly connected to the aspect ratio of the rod. From eq 5 we obtain

$$\frac{\omega_{br}^{(0)}}{\omega_{ext}^{(0)}} = \frac{\tau_0}{\pi}\left(\frac{L}{a}\right)\sqrt{\frac{(1 - \nu)}{(1 + \nu)(1 - 2\nu)}} \qquad (8)$$

This finding should enable the aspect ratio of the rod to be determined from a single measurement of its temporal response following thermal excitation. This predicted behavior will be examined in the Results and Discussion section.

Note that in practice the heating pulse is not instantaneous, and the amplitudes of the excited modes will depend on their period compared to the duration of the heating process.[11,12] Thus, even though the amplitude of the extensional mode in Figure 1 is much less than that of the breathing mode, the extensional mode may dominate the dynamics in a real experiment because of its much lower frequency. In addition, because the period of the breathing mode is proportional to the width of the rod, this

mode will be more prominent for samples of "fat" rods. Also note that for a polydisperse system of rods, the vibrational modes will be damped in a way that depends on both the polydispersity and the resonant frequency. For example, for a Gaussian distribution of rod lengths, it can be shown that the fundamental of the extensional mode will be damped by a $\exp(-(t/\tau)^2)$ factor, where the damping time τ is given by $\tau = \bar{L}\bar{T}/\sqrt{2}\pi\sigma$.[36] In this formula, $\bar{L}$ is the average length of the rods, σ is the standard deviation of the distribution, and $\bar{T} = 2\bar{L} \times \sqrt{\rho/E}$ is the average period for the sample.[36] Thus, for samples with similar polydispersities (similar values of $\sigma/\bar{L}$), samples of shorter rods (small $\bar{T}$) will have faster damping times than longer rods. Conversely, for a given sample, we expect the higher frequency breathing mode to damp more rapidly than the extensional mode (for equal polydispersity in length and width).

3. Experimental Apparatus and Techniques

Chemicals. Ascorbic acid, cetyltrimethylammonium bromide (CTAB), $HAuBr_4$ and $NaBH_4$ were supplied from Aldrich. $HAuCl_4 \cdot 3H_2O$ and trisodium citrate dihydrate were supplied from Sigma. Sodium chloride was supplied from Fluka. Cetyltrimethylammonium chloride (CTAC) and dodecyltrimethylammonium bromide (DTAB) were supplied from Kodak Specialty Chemicals. All reagents were used without further purification. Milli-Q water was used in all the preparations.

Synthesis of Au Nanorods. Gold nanorods were prepared using both the electrochemical method described by Wang et al.[17] and also using a modified version of the solution phase synthesis developed by Jana and Murphy.[23] For electrochemical synthesis, the cell consisted of a sacrificial gold anode ($10 \times 10 \times 1$ mm) and a platinum cathode ($10 \times 40 \times 1$ mm) maintained at a separation of 2 mm. An additional silver plate ($10 \times 10 \times 1$ mm) was placed behind the Pt electrode. The electrolyte was made up of 3 cm³ of a 0.08M solution of the CTAB and 10 mg of the cationic cosurfactant tetraoctylammonium bromide (TOABr). The Au colloidal solution thus obtained after electrolysis contained both spherical and rod-shaped particles. Centrifugation (3500 rpm, 20 min) removed a large fraction of the spheres from the suspernatant solution, and a further centrifugation step (12 000 rpm, 1 h) removed excess surfactant. This process yielded more polydisperse rods than those produced via solution phase synthesis, but rods with smaller widths could be prepared. The electrochemically produced samples are numbered 1–3, 5, and 9 in Table 1.

The seeded growth method in solution led to much narrower size distributions and allowed much more control over the aspect ratio of the gold particles. The original protocol from Jana and Murphy[23] was modified to minimize the creation of spheres.[37] The UV–vis absorption spectra were recorded on a Cary 5 UV–vis–NIR spectrophotometer. The mean size and dispersity of the gold rods were determined using a Philips CM-10 electron microscope at 100kV. A 10-μL volume of colloidal solution was pipetted onto carbon-coated copper grids. Spheres were not included in any histograms.

Transient Absorption Apparatus. The transient absorption experiments were conducted with a regeneratively amplified Ti:Sapphire laser system that has been described in detail

(36) Hartland, G. V. *J. Chem. Phys.* **2002**, *116*, 8048.
(37) Perez-Juste, J.; Liz-Marzán, L. M.; Mulvaney, P. *Adv. Funct. Mater.*, in preparation.

Table 1. Average aspect ratio ($\bar{\xi} = \overline{L/w}$), maximum of the longitudinal plasmon band (λ_{max}), average length ($\bar{L}$), average width ($\bar{w}$) and average vibrational period ($\bar{T}$) for the different gold nanorod samples examined in this work[a]

sample	$\bar{\xi}$	λ_{max} (nm)	$\bar{L}$ (nm)	$\bar{w}$ (nm)	$\bar{T}$ (ps)
1	2.7 ± 0.8	651	35 ± 10	13 ± 1	49 ± 2
2	3.0 ± 0.9	677	36 ± 10	12 ± 1	54 ± 2
3	3.5 ± 1.0	715	42 ± 10	12 ± 1	58 ± 2
4	2.23 ± 0.55	699	46 ± 6	20.7 ± 2.3	54.6 ± 1
5	2.1 ± 0.6	596	55 ± 15	26 ± 2	62 ± 2
6	2.81 ± 0.42	746	61 ± 5	21.5 ± 1.9	65.4 ± 1
7	3.29 ± 0.33	786	73 ± 4	22.1 ± 1.5	77.4 ± 1
8	3.34 ± 0.45	822	75 ± 6	22.4 ± 1.7	80.0 ± 1
9	5.5 ± 1.6	830	77 ± 20	14 ± 1	70 ± 2
10	4.05 ± 0.52	902	89 ± 7	22.2 ± 2.0	101.0 ± 1
11	4.75 ± 0.49	976	108 ± 7	22.8 ± 1.6	119.9 ± 1

[a] Samples 4, 6, 7, 8, 10, and 11 are high quality (relatively low polydispersity), and samples 1, 2, 3, 5, and 9 are considered to be low quality. The errors for $\bar{\xi}$, $\bar{L}$, and $\bar{w}$ represent the standard deviations obtained by fitting histograms of the parameter to a normal distribution.

elsewhere.[38,39] For the experiments described below, pump laser pulses at 400 nm with energies of approximately 0.1 μJ/pulse were used, and probe pulses in the visible to near-IR were obtained from a white-light continuum. The samples were contained in a 2 mm cuvette and the experiments were performed without flowing. The concentration of the sample was adjusted to give an absorbance at the pump laser wavelength of ~1. Care was taken to keep the pump laser power below the damage threshold for the sample—laser induced damage is easy to observe as it produces a dramatic color change in the sample.[40] We estimate that these experimental conditions produce temperature increases in the gold lattice on the order of 20−40 °C, after the electrons and phonons have reached equilibrium.[36] Fits to the modulated portion of the data, using a damped cosine function with a decaying offset, were performed using the "Solver" routine in *Microsoft Excel X for Mac*.

4. Experimental Results

Despite the care taken to purify these samples, the solutions produced contain a large number of spheres (~50%) and are polydisperse. The samples used in the time-resolved experiments can be roughly divided into two categories: high quality samples (low polydispersity) produced by the seed mediated growth technique, and low quality samples produced electrochemically. Representative TEM images of the high quality samples used in our experiments are presented in Figure 2. The average length ($\bar{L}$) and width ($\bar{w}$) for the different samples are (from the top): (a) $\bar{L} = 108 \pm 7$ nm, $\bar{w} = 22.8 \pm 1.6$ nm; (b) $\bar{L} = 89 \pm 7$ nm, $\bar{w} = 22.2 \pm 2.0$ nm; (c) $\bar{L} = 75 \pm 6$ nm, $\bar{w} = 22.4 \pm 1.7$ nm; (d) $\bar{L} = 73 \pm 4$ nm, $\bar{w} = 22.1 \pm 1.5$ nm; (e) $\bar{L} = 61 \pm 5$ nm, $\bar{w} = 21.5 \pm 1.9$ nm; and (f) $\bar{L} = 46 \pm 6$ nm, $\bar{w} = 20.7 \pm 2.3$ nm. The errors represent the standard deviation (500−1000 particles counted for each measurement). The average values and standard deviations were obtained by fitting histograms of the length or width to a Normal Distribution function. Detailed high-resolution TEM analysis has shown that the rods produced
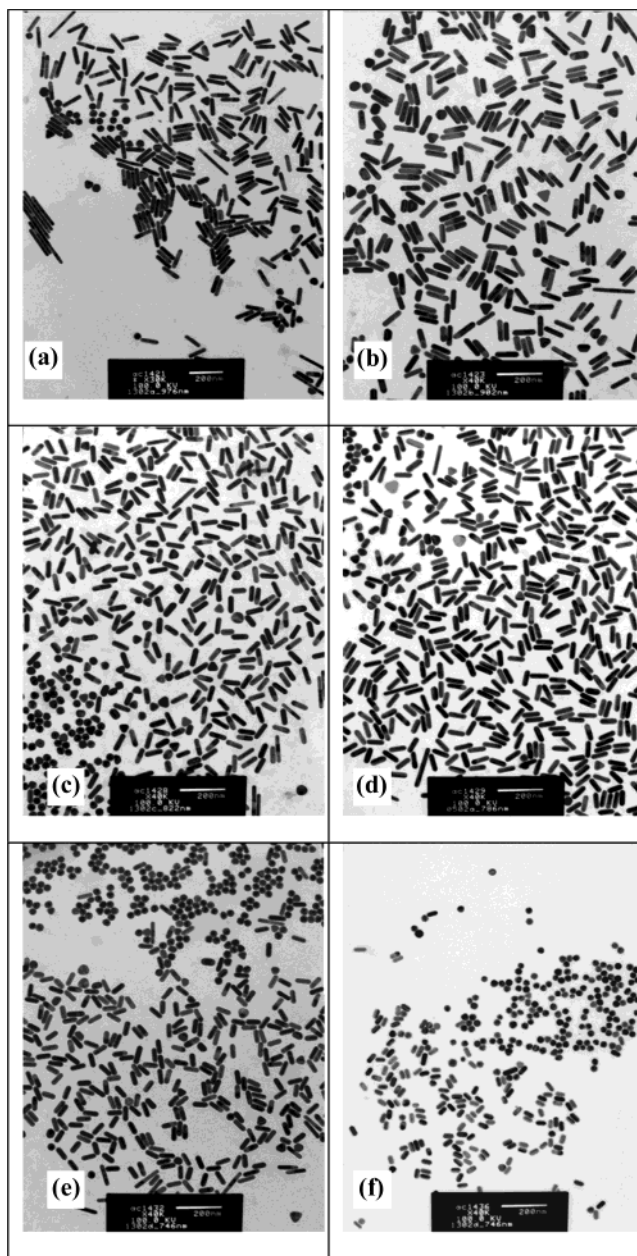
(38) Martini, I.; Hodak, J. H.; Hartland, G. V.; Kamat, P. V. *J. Chem. Phys.* **1997**, *107*, 8064.
(39) Hodak, J. H.; Martini, I. B.; Hartland, G. V. *J. Phys. Chem. B* **1998**, *102*, 6958.
(40) Link, S.; Burda, C.; Nikoobakht, B.; El-Sayed, M. A. *J. Phys. Chem. B* **2000**, *104*, 6152.

Figure 2. Representative TEM images of the gold nanorods used in our experiments. The images correspond (from top left) to the samples with average lengths of: (a) $\bar{L} = 108 \pm 7$, (b) $\bar{L} = 89 \pm 7$ nm, (c) $\bar{L} = 75 \pm 6$ nm, (d) $\bar{L} = 73 \pm 4$ nm, (e) $\bar{L} = 61 \pm 5$ nm, and (f) $\bar{L} = 46 \pm 6$ nm.

by the seed mediated growth technique are single crystals, that grow along a specific crystal direction.[41,42] The fact that the rods are single crystals can be seen in the low resolution TEM images in Figure 2: the rods typically appear as all light or all dark depending on the orientation of the lattice with respect to the electron beam.[43]

UV−visible absorption spectra of the high quality (seed mediated growth) samples are shown in Figure 3. The spectra show the characteristic longitudinal and transverse plasmon resonances that correspond to oscillation of the conduction electrons along the length or width of the rod.[29] The transverse

(41) Johnson, C. J.; Dujardin, E.; Davis, S. A.; Murphy, C. J.; Mann, S. *J. Mater. Chem.* **2002**, *12*, 1765.
(42) Nikoobakht, B.; El-Sayed, M. A. *Chem. Mater.* **2003**, *15*, 1957.
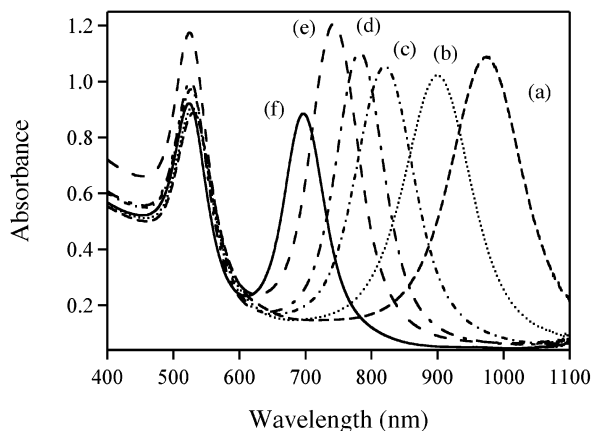(43) Wang, Z. L. *J. Phys. Chem. B* **2000**, *104*, 1153.

Figure 3. UV−visible absorption spectra of the "high quality" gold nanorod samples. The average lengths for the different spectra are as follows: (a) $\bar{L} = 108 \pm 7$, (b) $\bar{L} = 89 \pm 7$ nm, (c) $\bar{L} = 75 \pm 6$ nm, (d) $\bar{L} = 73 \pm 4$ nm, (e) $\bar{L} = 61 \pm 5$ nm, and (f) $\bar{L} = 46 \pm 6$ nm.

Figure 4. Transient absorption traces for high quality (seed mediated growth) samples with average lengths of (a) $\bar{L} = 46 \pm 6$ nm, (b) $\bar{L} = 61 \pm 5$ nm, (c) $\bar{L} = 75 \pm 6$ nm and (d) $\bar{L} = 89 \pm 7$ nm, for two different probe laser wavelengths. In all cases, the probe wavelengths presented lie on opposite sides of the longitudinal plasmon band of the sample. Note the different scale for the time axes in panel (d).

Figure 5. Transient absorption traces for low quality samples with average lengths of (a) $\bar{L} = 36 \pm 10$ nm and (b) $\bar{L} = 42 \pm 10$ nm for two different probe laser wavelengths. The probe wavelengths were chosen to lie on either side of the longitudinal plasmon band of the sample.

plasmon band appears at ca. 520 nm for all the samples, whereas, the longitudinal resonance appears between 600 and 1100 nm, depending on the aspect ratio. The different rod samples produced by the seed mediated growth technique have very similar widths (see Table), thus, the aspect ratio is mainly determined by the length of the rod. The degree of polydispersity in the samples can be qualitatively judged from the width of the spectra. Calculated spectra (no polydispersity) typically have fwhm of 0.08 eV in the visible/near-IR region.[29] This is also the width observed in Rayleigh scattering spectroscopy measurements for single nanorods.[44] The spectra in Figure 3 have a fwhm of ∼0.2 eV, approximately twice the width expected for a monodisperse sample. In contrast, the lower quality samples (which contain a similar percentage of spheres, but have much broader size distributions) have fwhm of ∼0.4 eV. In what follows, we present transient absorption results for both the high quality and low quality samples, even though the polydispersity in the low quality samples makes the analysis of the data much more difficult.

Note that the near-UV absorbance for the spectra in Figure 3 does not strongly depend on aspect ratio, which means that all the rods in the sample are equally excited by the 400 nm pump laser pulses. However, only the rods that have their longitudinal plasmon bands resonant to the probe laser will contribute to the signal.[30] In addition, the spheres do not significantly contribute to the transient absorption signal at the wavelengths used in these experiments.[36] Thus, even though ∼50% of the particles in the sample are spheres, we only monitor the rods in the transient absorption measurements presented below.

Representative transient absorption traces for different rod samples are presented in Figures 4−6. Figure 4 shows data from high quality samples with average lengths of (a) $\bar{L} = 46 \pm 6$ nm, (b) $\bar{L} = 61 \pm 5$ nm, (c) $\bar{L} = 75 \pm 6$ nm and (d) $\bar{L} = 89 \pm 7$ nm, for two different probe laser wavelengths. The traces presented correspond to experiments performed on opposite sides of the longitudinal plasmon band (i.e., red of the maximum versus blue of the maximum). In each case, the signal shows a fast component, which is attributed to energy transfer from the initially excited electron distribution into the phonon modes,
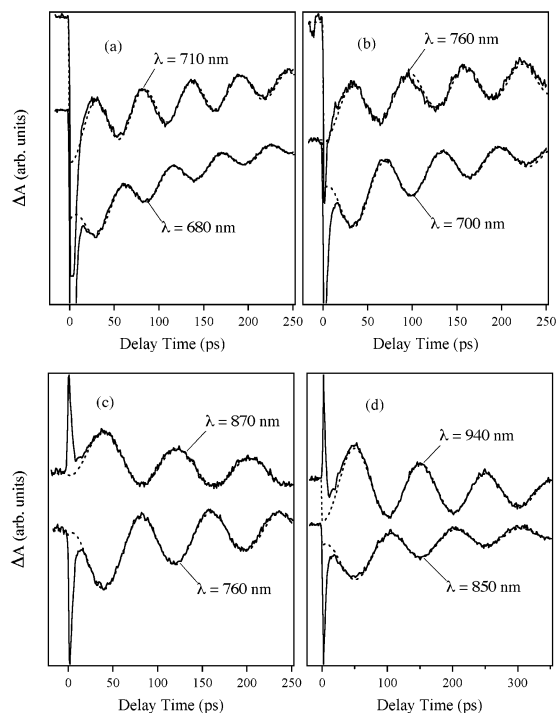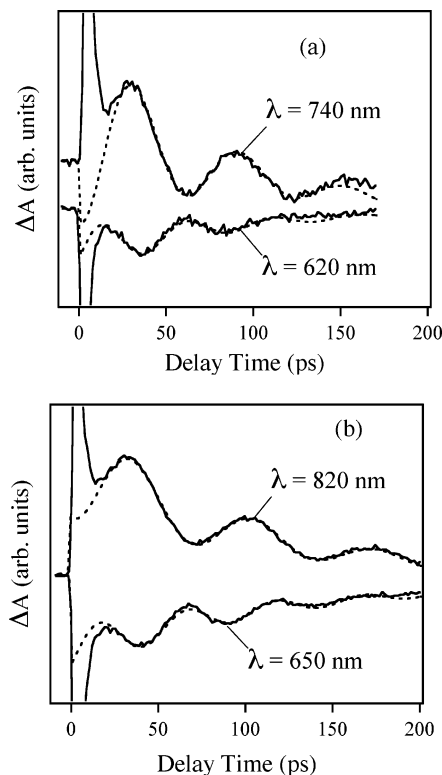
(44) Sönnichsen, C.; Franzl, T.; Wilk, T.; von Plessen, G.; Feldmann, J.; Wilson, O.; Mulvaney, P. *Phys. Rev. Lett.* **2002**, *88*, 077 402.

electron−phonon (e−ph) coupling,[11,12] and a modulation due to the coherently excited vibrational modes. Note that in several
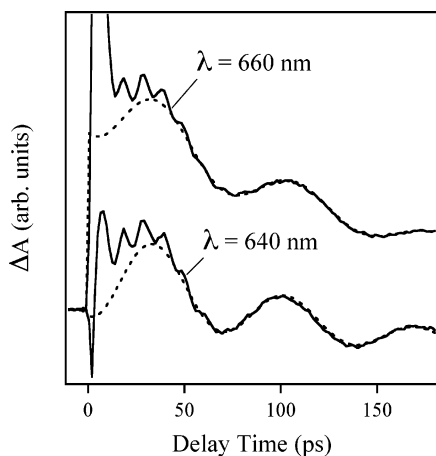
Figure 6. Transient absorption data for the low quality sample with an average length of $\bar{L} = 55 \pm 15$ nm, for probe laser wavelengths of $\lambda = 640$ nm and $\lambda = 660$ nm.

cases, the signal from the hot electron distribution has been truncated to highlight the modulated portion of the data. The modulation is superimposed on a slowly varying background, which corresponds to heat dissipation to the environment.[31−33,45,46] Also shown in the figures are fits to the experimental data using a damped cosine function.

There are several points to note about the modulations. First, for these high quality samples the period is similar for different probe wavelengths. Second, the damping time is relatively long compared to that from the low quality samples, see Figure 5. Third, the modulations are ∼180° out-of-phase for probe wavelengths on opposite sides of the longitudinal plasmon band. This implies that the signal arises from a periodic shift in the position of the longitudinal plasmon band— similar to what occurs for spherical particles.[36]

Figure 5 shows transient absorption data for several low quality samples. The general features—fast initial decay due to e−ph coupling with modulations superimposed on a slowly varying background—are similar. However, there are key differences for the low quality samples compared to the high quality samples: (i) the modulations are much more strongly damped; (ii) the period now depends on the probe wavelength; and (iii) the phase difference between traces on opposite side of the longitudinal plasmon band is now only ∼60°. All of these effects are consequences of polydispersity. As we showed in our previous communication, the period changes with probe laser wavelength because different length rods in the sample absorb at different spectral regions.[30] The phase and damping are complicated effects that will be dealt with in detail elsewhere.

Figure 6 shows transient absorption data for the low quality $\bar{L} = 55 \pm 15$ nm sample at two different probe wavelengths. The important point to note from this figure is that these traces show fast modulations at early times with a period of ∼11 ps (the period was determined by fitting data collected over a shorter time range), as well as slower modulations. The period of the slower modulations is 68 ps for the $\lambda = 640$ nm trace and 71 ps for the $\lambda = 660$ nm trace. The fast modulations can be observed for some of the other samples, but are not as
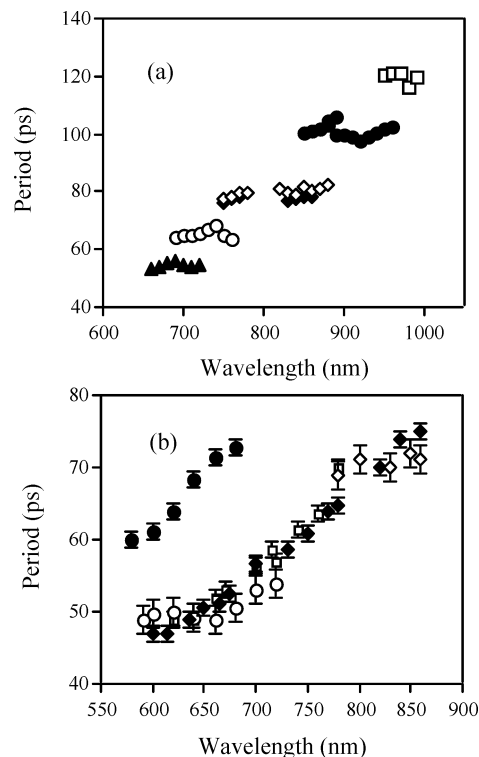
(45) Roberti, T. W.; Smith, B. A.; Zhang, J. Z. *J. Chem. Phys.* **1995**, *102*, 3860.
(46) Ahmadi, T. S.; Logunov, S. L.; El-Sayed, M. A. *J. Phys. Chem.* **1996**, *100*, 8053.

Figure 7. Period versus probe laser wavelength for all the different samples examined to date. (a) High quality samples. The different symbols indicate average lengths of $\bar{L} = 46 \pm 6$ nm (▲), $\bar{L} = 61 \pm 5$ nm (○), 73 ± 4 (◆), $\bar{L} = 75 \pm 6$ (◇), $\bar{L} = 89 \pm 7$ nm (●) and $\bar{L} = 108 \pm 7$ (□). The error bars are contained within the symbol. (b) Low quality samples. The different symbols indicate average lengths of $\bar{L} = 55 \pm 15$ nm (●), $\bar{L} = 35 \pm 10$ nm (○), $\bar{L} = 36 \pm 10$ nm (□), $\bar{L} = 42 \pm 10$ nm (◆), and $\bar{L} = 77 \pm 20$ nm (◇). Note the different horizontal and vertical scales for each panel.

pronounced as in the data in Figure 6 (and, therefore, not analyzable). We do not believe that this signal arises from the spherical particles in the sample: the fast modulation disappears as we tune the probe laser toward the transverse plasmon band, contrary to what we would expect for spheres (spherical particles show stronger signals near 530 nm). As will be shown below, this period is consistent with the breathing mode of these rods.

In Figure 7 the period versus probe wavelength results for the slower modulations are presented for all the samples investigated to date. Figure 7a shows data for the high-quality samples, and Figure 7b shows data for the low-quality samples. For a given high-quality sample, the period is relatively insensitive to the probe wavelength. In contrast, for the low-quality samples the measured period clearly increases as the probe laser is tuned from the blue to the red. Again, this arises because longer probe wavelengths interrogate longer rods in the polydisperse samples. The increase in period with wave-length thus demonstrates that the vibrational period is propor-tional to the length of the rod. In the high-quality samples, all of the rods are about the same length, so there is no wavelength dependence of the period for a given sample. How the period changes with wavelength is, therefore, a clear indicator of the quality of the samples.

The period versus probe wavelength data in Figure 7b fall onto two curves. The sample with an average length of $\bar{L} = 55 \pm 15$ is on one curve, and the samples with lengths of $\bar{L} = 35 \pm 10$, $\bar{L} = 36 \pm 10$, $\bar{L} = 42 \pm 10$ and $\bar{L} = 77 \pm 20$ are on another curve. This difference arises because the rods in the sample with $\bar{L} = 55$ are approximately 2× wider than the rods
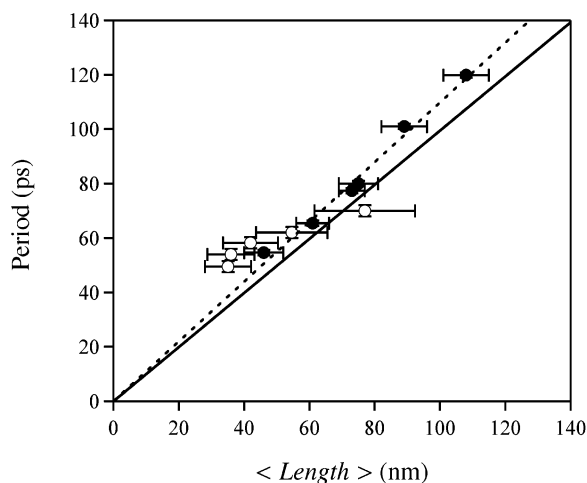
Figure 8. Average period versus average length for the Au nanorods examined in this work. The open symbols indicate the low quality samples, and the closed symbols show the high quality samples. The solid line is the calculated period for the fundamental extensional vibrational mode, see text for details. The dashed line represents a fit to the data assuming that the period is proportional to the length. The horizontal error bars reflect the polydispersity in the samples.

in the other samples, see Table 1. Specifically, the probe laser interrogates rods according to their aspect ratio, but the periods measured in our experiments depend on the length. Thus, samples with different widths will give different periods for the same probe wavelength. Otherwise stated, optical probes are unable to distinguish between samples with identical aspect ratios, but different lengths and widths. However, as we will show below, a combination of steady-state and time-resolved spectroscopy measurements can completely determine the dimensions (aspect ratio and length) of the nanorods.

5. Discussion

To compare the different samples, the experimental data in Figure 7 was used to determine the vibrational period corresponding to the *average rod* in the sample, that is, the rods with the average dimensions as determined by TEM. For the high-quality samples, this is easy to do: we simply average the periods from the different probe wavelength experiments (as there is no clear trend in the period versus wavelength). For the low-quality samples, the wavelength dependence of the period makes this more difficult. For these samples, we assume that the average rod corresponds to the maximum in the longitudinal plasmon band of the sample (λ_{max}). However, it is hard to experimentally observe modulations when $\lambda_{probe} \approx \lambda_{max}$, because at this wavelength the signal due to the coherently excited vibrational modes changes sign—which means that the magnitude becomes very small. Thus, data recorded on either side of the maximum in the longitudinal plasmon band were used to estimate the period corresponding to the average rod for the low-quality samples. The results are tabulated in Table 1 for all the samples, along with the average length, width, and aspect ratio of the nanorods determined by TEM analysis, and the values of λ_{max}. In Table 1, samples 4, 6, 7, 8, 10, and 11 are considered high quality, and the others are low quality.

In Figure 8, the average periods are plotted versus the average length determined by TEM. The low-quality samples are indicated by the open symbols. Note that the data from all of the samples now falls onto the one curve (within error), despite

the variety of different widths for the different samples. Also shown in Figure 8 is the period of the fundamental extensional mode of the rods calculated using eq 5a (solid line). The values of E and ρ used were $E = 0.78$ Mb and $\rho = 19.3$ g/cm³— appropriate for Au at temperatures slightly above room temperature.[47] The reasonable agreement between the calculated and experimental results shows that the dominant vibrational mode excited in these experiments is the fundamental extensional mode. This is the major conclusion from this paper.

The dashed line in Figure 8 shows a fit to the data assuming that the period is proportional to the length. As expected, the fit is consistent with the analytical result of eq 5a. Only rods with lengths greater than 40 nm were included in this fit, as these rods correspond to the $L/a \gg 1$ condition used to derive eq 5a. Also, the low quality sample with $\bar{L} = 77 \pm 20$ nm was not included in the fit, as the period for this sample deviates significantly from the results for the other samples. This analysis yields a value of Young's modulus of $E = 0.64 \pm 0.08$ Mb for $\rho = 19.3$ g/cm³, slightly lower than the known value for bulk gold.

There are several reasons why Young's modulus for the nanorods could be different from the value for bulk gold: (1) contributions from the surface energy to the overall cohesive energy of the rods; (2) a change in the elastic properties of the material due to quantum confinement effects in the electronic states; and/or (3) the measured value of E is different from the bulk value because the nanorods are single crystals and not elastically isotropic. Of these three possibilities we think that the third is the most likely: our experiments on the extensional mode probe Young's modulus along the axial direction of the rod. Because the rods grow along a specific crystal direction,[41,42] the value of Young's modulus measured will be different to the value for bulk, polycrystalline gold.[47,48] In addition, at room temperature surface energy and quantum confinement effects are only important for gold particles smaller than a few nanometers.[49,50] Thus, these effects are unlikely to play a role for our particles which have dimensions over 20 nm.

Finally, we examine the fast modulations for the $\bar{L} = 55 \pm 15$ sample which are clearly visible in Figure 6. In this figure, the period of the fast modulations is 11 ± 1 ps for both probe wavelengths. In comparison, the slower modulations have a period of 68 ± 2 ps for $\lambda = 640$ nm, and 71 ± 2 ps for $\lambda = 660$ nm. The analytical theory presented above predicts that for gold (Poisson's ratio $\nu = 0.42$) the ratio of frequencies for the fundamental breathing and extensional modes should be

$$\frac{\omega_{br}^{(0)}}{\omega_{ext}^{(0)}} = 2.32 \times \zeta \qquad (9)$$

where ζ is the aspect ratio of the nanorod. The value of ζ interrogated in the experiments depends on the probe wavelength, and is not necessarily the same as the average aspect ratio $\bar{\zeta}$ of the sample. For the low-quality nanorods produced by the electrochemical technique (Figures 5 and 6), the

(47) Simmons, G.; Wang, H. *Single-Crystal Elastic Constants and Calculated Aggregate Properties: A Handbook*; The MIT Press: Cambridge, 1971.
(48) Landau, L. D.; Lifshitz, E. M. *Theory of Elasticity*; 2nd ed., Pergamon Press: Oxford, 1970.
(49) Buffat, P.; Borel, J.-P *Phys. Rev. A* **1976**, *13*, 2287.
(50) Alvarez, M. M.; Khoury, J. T.; Schaaff, T. G.; Shafigullin, M. N.; Vezmar, I.; Whetten, R. L. *J. Phys. Chem. B* **1997**, *101*, 3706.

wavelength of the longitudinal plasmon resonance is related to the aspect ratio by $\lambda_{max} = (67 \pm 5) \times \zeta + (469 \pm 16)$. This relationship was determined by comparison between the experimental spectra and the TEM results, see Table 1. Note that the relationship between λ_{max} and aspect ratio is different for the high quality samples, presumably because the different synthetic procedures produce different surfactant coatings.

Using the above relationship, the $\lambda = 640$ nm probe pulses should interrogate rods with an aspect ratio of $\zeta \approx 2.55 \pm 0.3$, and the $\lambda = 660$ nm pulses should interrogate rods with an aspect ratio of $\zeta \approx 2.85 \pm 0.3$. Thus, eq 9 predicts that the ratio of frequencies should be $\omega_{br}^{(0)}/\omega_{ext}^{(0)} \approx 5.9 \pm 0.6$ for a probe wavelength of 640 nm, and $\omega_{br}^{(0)}/\omega_{ext}^{(0)} \approx 6.6 \pm 0.6$ for a probe wavelength of 660 nm. In comparison, analyses of the transient absorption data give ratios of 6.2 ± 0.6 for the 640 nm probe experiment, and 6.4 ± 0.6 for the 660 nm probe experiment.

The reasonable agreement (within experimental error) between the calculated and experimental ratios of the fundamental frequencies supports the conclusion that the fast modulation is the fundamental breathing mode of the rod. Note that the fast oscillations decay much more rapidly in time than the slower oscillations, which is consistent with the damping being dominated by polydispersity.[36] The breathing mode is not observed for the other nanorod samples presumably because these samples are thinner. For thinner nanorods, the period of the breathing mode is faster, which means that it is not effectively excited by the laser-induced heating/expansion process.[12]

6. Summary and Conclusions

This combined experimental/theoretical study establishes that laser induced heating of cylindrical nanorods excites both the extensional and breathing vibrational modes of the rod. Specifically, transient absorption experiments for gold nanorod samples with average aspect ratios (length/width) between 2 and 6, and lengths between 30 and 110 nm, show pronounced modulations with a period of 40 to 120 ps (depending on the sample and the probe wavelength), which are assigned to the extensional mode. Faster modulations with a period of ~11 ps are also observed for a sample with an average length of 55 nm and a width of 26 nm. This signal is assigned to the breathing mode of the rods. The measured periods are in good agreement with the theoretical model, which is derived using classical continuum mechanics in the limit where the length of the rod greatly exceeds its radius. The relative contributions of the different vibrational modes to the rod deformation were also calculated, assuming that the heating/expansion process is instantaneous. The results suggest that most of the amplitude should be contained in the breathing mode. However, because the fundamental extensional mode is much lower in frequency, this mode dominates the dynamics in the experiments, which have a finite heating time. The time scale for heating in the experiments depends on the electron−phonon coupling constant, and is several picoseconds for gold.

Note that the frequency of the breathing mode depends on the width of the rod, whereas, the period of the extensional mode

simply depends on its length (i.e., the ratio of the fundamental breathing and extensional mode frequencies only depends on the aspect ratio). Consequently, in transient absorption experiments where both the breathing and extensional modes can be observed, the measured periods completely determine the dimensions of the rod (i.e., length and width). In contrast, measurements of the optical absorption spectra only yield the aspect ratio of the rod. Thus, these experiments are potentially valuable for determining the dimensions of nanorods in situ. In general, the extensional mode is easier to observe than the breathing mode. Thus, for practical applications, the best approach for optically measuring the dimensions of nanorods is to use steady-state spectroscopy to determine the aspect ratio, and time-resolved spectroscopy to determine the length.

It is interesting to compare these results to the recent work on spherical nanoparticles.[1−9,11,12] For spheres, the expansion coordinate exactly correlates with the symmetric breathing mode, which means that only the radially symmetric (breathing) modes are excited by the rapid heating/expansion process. In contrast, for nonspherical particles (the rods in our experiments and the ellipsoids of ref 7) multiple types of vibrational modes are excited. Theoretically, the vibrational modes of an isotropic elastic sphere can be treated *exactly* using continuum mechanics, and the results are well-known.[13,14] The good agreement between the experimental and theoretical results in this study, establishes that the present approximate theory (derived for cylinders of high aspect ratio) is applicable to the nanorods synthesized by current techniques.[17,23]

The experimental results were also used to estimate Young's modulus of the nanorods. Assuming a density of Au of $\rho = 19.3$ g/cm^3, we obtain a value of Young's modulus of $E = 0.64 \pm 0.08$ Mb. This is consistent with, but slightly lower than, the known value for bulk Au of $E = 0.78$ Mb.[47] Several possible reasons for the different value of Young's modulus for the nanorods compared to bulk gold were considered. We believe that the most likely reason for this difference is that the nanorods are single crystals and not elastically isotropic. Specifically, our experiments probe Young's modulus along the axial direction of the rod. For the nanorods produced by the seed mediated growth technique, the axial direction corresponds to a definite crystal direction.[41,42] The measured value of Young's modulus will, therefore, be different to the tabulated value for bulk, polycrystalline gold.[47,48]

Supporting Information Available: Equations 4a, 4b, and 5b, which describe deformation, eigenvalues, and frequencies, respectively, for the breathing modes of the nanorods, are derived in the Supporting Information that accompanies this paper. This material is available free of charge via the Internet at http://pubs.acs.org.

JA037443Y